COBEM 2023 27TH INTERNATIONAL CONGRESS OF MECHANICAL ENGENEERING

ABCM Brazilian Society of Mechanical Sciences and Engineering
27th ABCM International Congress of Mechanical Engineering
December 04-08, 2023, Florianópolis-SC, Brazil

COB-2023-1422
DYNAMIC ANALYSIS OF A MULTI-SHAFT GEARED SYSTEM SUPPORTED BY HYDRODYNAMIC BEARINGS

João Henrique dos Santos de Pontes
Gregory Bregion Daniel
Tiago Henrique Machado
School of Mechanical Engineering, University of Campinas. Mendeleyev Street, 200, Campinas - SP - 13083-860
joaohspontes@gmail.com; gbdaniel@fem.unicamp.br; tiagohm@fem.unicamp.br

Abstract.*In this work, a model of multi-shaft geared system is developed using the finite element method to simulate dynamic response of a wind turbine-like multi-shaft system. Shafts are modeled using Timoshenko's beam element with 5 degrees of freedom per node, and connected by helical gears that couple all degrees of freedom of the system, and introduce a time-varying gearing stiffness. To evaluate the influence of bearing effects on the rotating system's dynamic response, different types of bearings are considered in the numerical simulations. The effects of hydrodynamic journal bearings are discussed in comparison to simpler rolling bearings model. The rotating system is analyzed both in the frequency and the time domain. Modal analysis is performed to predict the system's natural frequencies and obtain Campbell diagrams, presenting the critical speeds of the multi-shafts of the rotating system. Finally, time responses are obtained using Newmark's time integration method and a Fast Fourier Transform (FFT) is used to decompose time vibration signals and reveal internal gearboxes frequencies and their typical harmonics, associated to tooth meshing. The results obtained in this work provide important contributions related to the bearings effects on the dynamic response of a multi-shaft geared system, thus allowing to investigate possible improvements related to gearboxes, which are critical components for the performance of wind turbines.*

Keywords: *dynamic analysis, hydrodinamic bearings, gearbox coupling, wind turbines*

1. INTRODUCTION

The increasingly urgent demand for public policies that promote the improvement of environmental and climatic conditions inevitably encounters the model of energy generation and usage by society. Wind energy, understood as the kinetic energy of moving air masses (Agência Nacional de Energia Elétrica, 2005), emerges as one of the clean energy production alternatives with great potential.

Specifically in Brazil, wind energy generation has been gaining prominence in recent years as one of the fastest-growing energy sources (Pinto and dos Santos, 2019). Data from the 2021 Wind Energy Generation Bulletin (the latest available) from the Brazilian Wind Energy Association (ABEEólica) confirms that this was a remarkable year for the wind energy sector. Brazil ended the year 2021 with 795 wind farms and 21.6 GW of installed capacity, representing a 21.5% growth in capacity compared to December 2020 (Associação Brasileira de Energia Eólica e Novas Tecnologias, 2021). In the same year, 110 new wind farms were installed, adding a total of 3.8 GW of new capacity, setting a record for installations in a single year in Brazil. This positioned the country as the third-largest installer of wind power generators in the world and the sixth-ranked in terms of global installed capacity (Global Wind Energy Council, 2021). The year concluded with an investment of USD 5.15 billion in the wind energy sector, representing 44% of investments made in renewable energy sources (Bloomberg New Energy Finance, 2021).

Horizontal axis wind turbines are chosen as the object of study for this work because they represent the majority of wind turbines installed in commercially operated wind farms worldwide. In simplified terms, this type of wind turbine consists of a supporting tower, coupled with a structure called the nacelle, a rotor with blades, a gearbox, and an electrical generator (Agência Nacional de Energia Elétrica, 2005).

In the field of rotor dynamics, the study of systems based on wind turbines has the distinguishing feature of having a speed multiplier composed of multiple shafts coupled via gearing, which introduce a time-varying stiffness on the system. In this context, the present work aims to study the influence of hydrodynamic bearings on a multi-shaft power train system of a horizontal-axis wind turbine, comparing the dynamic response of the system when supported by rolling bearings.

2. Modeling

The rotating system in this work was modeled using the finite element method, in which the system is divided into a finite number of elements connected to each other by nodes. In this study, each node has 5 degrees of freedom, corre-

sponding to displacements in X and Y coordinates, as well as rotations around X, Y, and Z axes (see Figure 1).

The degree of freedom for axial translation is disregarded because, in horizontal axis wind turbines, the dominant contribution to axial loading is due to the wind force on the blades, which is supported by an axial bearing located next to the blades, prior the first radial support bearing. The axial load resulting from helical gears can be neglected because the herringbone configuration cancels out the axial forces from the gearing pair.

This section presents details of the modeling for each type of element used in the study.

2.1 Shaft Element

The shaft element used in this work consists of a Timoshenko beam element, which takes into account the shear effects in the cross-sections. It was originally modeled by Nelson (1980) with 4 degrees of freedom per node. Subsequently, the effects of inertia and rotational deformation were added by Rao *et al.* (1998) to obtain a beam element with 5 degrees of freedom per node, as shown in Fig 1.

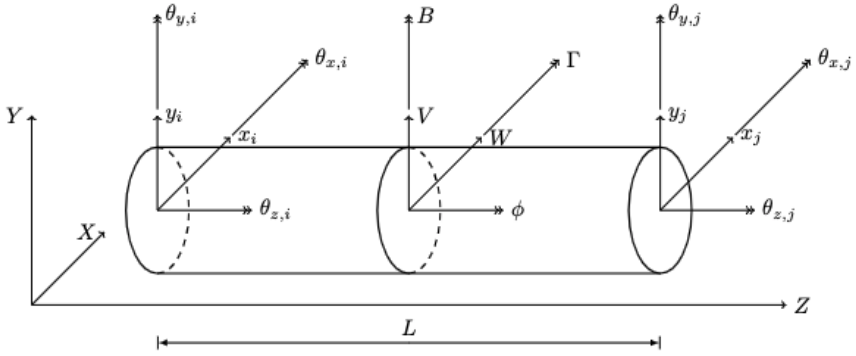

Figure 1: Shaft element and its coordinate system.

The equation of motion for the shaft element is given by:

$$[M^s]\{\ddot{q}^s\} + (\Omega[G^s] + [C^s])\{\dot{q}^s\} + [K^s]\{q^s\} = \{F^s\} \tag{1}$$

where $[M^s]$, $[G^s]$, $[C^s]$, and $[K^s]$ are the mass, gyroscopic, damping, and stiffness matrices of the beam element, respectively, obtained in Rao *et al.* (1998). $\{q^s\}$ is the vector of generalized displacements, shown in Eq. 2, and $\{F^s\}$ is the vector of external forces.

$$\{q^s\} = \begin{Bmatrix} x_i & y_i & \theta_{x,i} & \theta_{y,i} & \theta_{z,i} & x_j & y_j & \theta_{x,j} & \theta_{y,j} & \theta_{z,j} \end{Bmatrix}^t \tag{2}$$

2.2 Disk Element

The disk element used in this work is a rigid disk element with 5 degrees of freedom, as proposed by (Rao *et al.*, 1998). Its equation of motion in the matrix form is given by:

$$\left[M^d\right]\left\{\ddot{q}^d\right\} + \Omega\left[G^d\right]\left\{\dot{q}^d\right\} = \left\{F^d\right\} \tag{3}$$

where $\left[M^d\right]$ and $\left[G^d\right]$ are the mass and gyroscopic matrices of the disk element, respectively. $\left\{q^d\right\}$ is the vector of generalized displacements, and $\left\{F^d\right\}$ is the vector of external forces.

2.3 Bearing Elements

The bearing elements used in this work are modeled as a combination of springs and dampers, as illustrated in Fig. 2, and also used by Rao *et al.* (1998), Macedo (2017), and Visnadi (2022). The effects are included in the model at a single node, with equivalent coefficients of damping and equivalent stiffness. Only the terms related to translation are considered, so the equation of motion becomes:

$$\left[C^b\right]\left\{\dot{q}^b\right\} + \left[K^b\right]\left\{q^b\right\} = \left\{F^b\right\} \tag{4}$$

where the damping and stiffness matrices are given by:

$$[C_b] = \begin{bmatrix} c_{xx} & c_{xy} & 0 & 0 & 0 \\ c_{yx} & c_{yy} & 0 & 0 & 0 \\ 0 & 0 & 0 & 0 & 0 \\ 0 & 0 & 0 & 0 & 0 \\ 0 & 0 & 0 & 0 & 0 \end{bmatrix} \tag{5}$$

$$\left[K^b\right] = \begin{bmatrix} k_{xx} & k_{xy} & 0 & 0 & 0 \\ k_{yx} & k_{yy} & 0 & 0 & 0 \\ 0 & 0 & 0 & 0 & 0 \\ 0 & 0 & 0 & 0 & 0 \\ 0 & 0 & 0 & 0 & 0 \end{bmatrix} \tag{6}$$

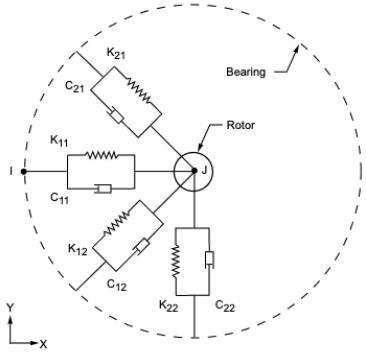

Figure 2: Bearing element illustration (Ansys, 2018)

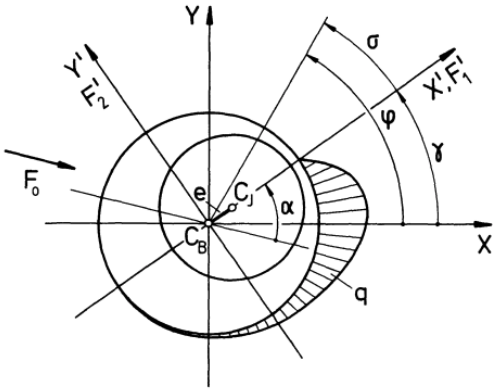

Figure 3: Forces actuating on a stady-state journal bearing (Kramer, 1993)

In the case of roller bearings, the stiffness and damping factors do not vary and are direct input. On the other hand, journal bearings have the characteristic of varying stiffness and damping depending on the rotational speed. To determine the equivalent damping and stiffness coefficients of hydrodynamic bearings, it is necessary to first obtain the oil film pressure distribution, which involves several fluid dynamics differential equations to be solved. For this reason, there are several simplifications that facilitate the calculation of hydrodynamic bearing coefficients. In this work, the method proposed by Kramer (1993) is used, which employs the simplifying assumption for short bearings (L/D < 0.5). Figure 3 illustrates the pressure distribution of the lubricating fluid and the resulting forces acting on a hydrodynamic bearing operating in a steady-state condition.

2.4 Gearing Element

The gearing elements used in this study are based on the work of Kubur *et al.* (2004), as illustrated in Fig. 4. In this model, the gears i (index of the first gear) and j (index of the second gear in the meshed pair) behave as two rigid disks coupled by a linear spring, where the stiffness represents the rigidity due to tooth contact.

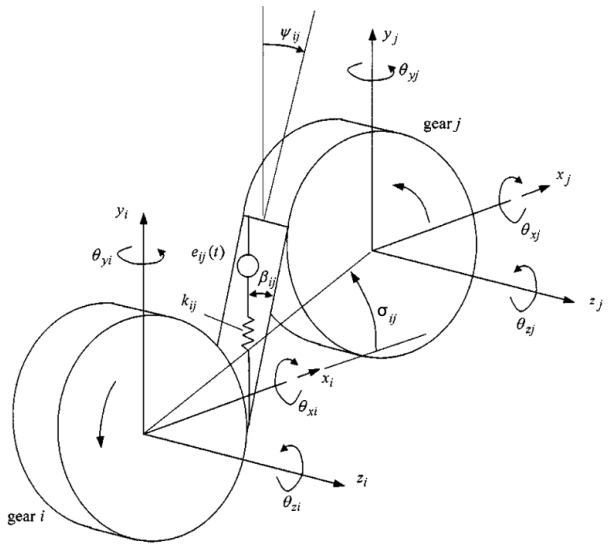

Figure 4: Three-dimensional model of a pair of helical gears (Kubur *et al.* (2004))

To model the gearing stiffness, it is necessary to define some geometric relations and relevant angles. The normal pressure angle α_n and the helix angle β are provided by the user as gear properties. From the positions of the nodes where the gears are applied, σ can be defined as the angle in the XY plane between the gear centers.

As well as the shaft and disk models, each gearing element node has 5 degrees of freedom, with axial translation (Z-axis) being the only DOF neglected in the modeling. Therefore, the equation of motion in matrix form is given by:

$$[M^g]\{\ddot{q}^g\} + \Omega\,[G^g] + [K^g]\{q^g\} = \{F\} \tag{7}$$

with the vector of generalized displacements given by:

$$q^g = \begin{Bmatrix} x_i & y_i & \theta_{xi} & \theta_{yi} & \theta_{zi} & x_j & y_j & \theta_{xj} & \theta_{yj} & \theta_{zj} \end{Bmatrix}^t \tag{8}$$

The mass matrix of gearing element is equivalent to two mass matrix of a rigid disk element, as shown in Section 2.2, coupled in the main diagonal:

$$[M^g] = \begin{bmatrix} \left[M_i^d\right] & [0] \\ [0] & \left[M_j^d\right] \end{bmatrix} \tag{9}$$

where $\left[M_i^d\right]$ and $\left[M_j^d\right]$ are the mass matrices of disk element regarding respectively the gear i and j, with the pitch diameter being considered the external diameter of its equivalent disk.

Although the modeling proposed by Kubur *et al.* (2004) and used by Macedo (2017) does not mention the gyroscopic effect in the gear elements, it is chosen to include the gyroscopic matrix of the gearing element analogously to the mass matrix: by diagonally coupling the individual gyroscopic matrices of each gear modeled as a rigid disk. Thus, following the approach proposed by Rao *et al.* (1998), the gyroscopic matrix for the geared pair element is given by:

$$[G^g] = \begin{bmatrix} \left[G_i^d\right] & [0] \\ [0] & \left[G_j^d\right] \end{bmatrix} \tag{10}$$

Finally, the gearing stiffness matrix, which couples all degrees of freedom of the gearing pair, is given by:

$$[K^g] = k \begin{bmatrix} [K_{1,1}^g] & [K_{1,2}^g] \\ [K_{2,1}^g] & [K_{2,2}^g] \end{bmatrix} \tag{11}$$

where $[K_{1,1}^g]$, $[K_{1,2}^g]$, $[K_{2,1}^g]$ and $[K_{2,2}^g]$ are coupling matrices obtained in Kubur *et al.* (2004). Although capable of modeling the geared pair by coupling all degrees of freedom of the gearing pair when the gears are helical, the model proposed by Kubur *et al.* (2004) treats the stiffness k between the two gears as a linear spring. On the other hand, due to the variation of the number of teeth in contact during the gearing process, it is reasonable to assume that this stiffness exhibits some kind of variation over time.

In this work the tooth contact stiffness is modelled according to Cai (1995), and the stiffness of a helical gear pair takes the form of an cubic exponential as:

$$k(X) = k_p \exp\left(C_a |X|^3\right) \tag{12}$$

where C_a is a coefficient obtained empirically, k_p is the peak stiffness (maximum stiffness) of the gear pair, and X is the relative position of the gears.

The term C_a is defined as:

$$C_a = 0.322(\beta - 5) + \left[0.23\left(\frac{b}{h}\right) - 23.26\right] \tag{13}$$

where β is the value of the helix angle in degrees, b is the face width of the gears, and h is the tooth height. The relative position of the gears, X, is calculated as:

$$X = \frac{\bar{X} - 0.5\varepsilon_\gamma P_{bt}}{1.125\varepsilon_\alpha P_{bt}} \tag{14}$$

where ε_γ is the total contact ratio, P_{bt} is the transverse base pitch, ε_α the transverse contact ratio and $\bar{X}$ is a term to quantify the total stiffness of the N meshing toot pair along the contact line (He *et al.*, 2007):

$$k(\bar{X})_{\text{total}} = \sum_{i=0}^{N-1} k_p \exp\left(C_a \left|\frac{\bar{X} - 0.5\varepsilon_\gamma P_{bt}}{1.125\varepsilon_\alpha P_{bt}}\right|^3\right) \tag{15}$$

with

$$\bar{X} = mod(L_a, P_{bt}) + (N - 1 - i)P_{bt} \tag{16}$$

where L_a is the action line meshing length

$$L_a = \varepsilon_\gamma P_{bt} \tag{17}$$

and N is the number of gearing tooth pair meshing along the contact line, given by:

$$N = \lceil \varepsilon_\gamma \rceil \tag{18}$$

Finally, the peak stiffness of the gear pair is given by (Cai, 1995):

$$k_p = \frac{b}{c_0 + c_1\left(\frac{1}{z_{v,1}} + \frac{1}{z_{v,2}}\right) + c_2\left(\frac{y_1}{z_{v,1}} + \frac{y_2}{z_{v,2}}\right) + c_1\left(\frac{1}{z_{v,1}^2} + \frac{1}{z_{v,2}^2}\right) + c_4\left(C_{y1} + C_{y2}\right) + c_5\left(C_{y1}^2 + C_{y2}^2\right)} \tag{19}$$

where z_v and Cy are, respectively, the virtual number of teeth and the center distance modification factor; c_0 is the theoretical deflection of a pair of meshed teeth, and the coefficients c_1, c_2, c_3, c_4, and c_5 are obtained by least squares fitting from experimental data, and their values are:

$$c_0 = \frac{2.25}{\left[-0.166\left(\frac{b}{h}\right) + 0.08\right](\beta_\circ - 5) + 44.5} \tag{20}$$

$$c_1 = -0.00854 \tag{21}$$

$$c_2 = -0.11654 \tag{22}$$

$$c_3 = 2.9784 \tag{23}$$

$$c_4 = -0.00635 \tag{24}$$

$$c_5 = 0.00529 \tag{25}$$

3. Dynamic Analysis

After determining the elementary matrices for each element in the system, the global global mass, gyroscopic, damping, and stiffness matrices of the system are assembled according to each element degree of freedom. These global matrices compose the global equation of motion, given by:

$$[M]\{\ddot{x}\} + (\Omega[G] + [C])\{\dot{x}\} + [K]\{x\} = \{f\} \tag{26}$$

and this equation is the basis for dynamic analysis. This section presents the methodology used in the three distinct types of dynamic analysis performed on this work.

3.1 Modal Analysis

Once the equation of motion has been obtained in its standard matrix form (Eq. 26), a series of parameters can be obtained from the modal analysis of the system. The natural frequencies, mode shapes, and damping ratios represent the modal parameters of the system, which characterize the system's dynamic behavior. These parameters can be obtained by solving the characteristic polynomial or by analyzing the dynamic matrix of the system represented in the state-space model. In the Finite Element Method formulation, it is more practical to use the dynamic matrix $[A]$ approach.

In the case of rotor dynamics, the dynamic matrix $[A]$ of the system is given by

$$[A] = \begin{bmatrix} [0] & [I] \\ -[M]^{-1}[K] & -[M]^{-1}(\Omega[G] + [C]) \end{bmatrix} \tag{27}$$

where the matrices $[M]$, $[G]$, $[C]$ and $[K]$ represent the global mass, gyroscopic, damping, and stiffness matrices of the system, respectively.

As can be observed, obtaining the modal parameters depends on the rotational speed of the system Ω. In the case of multi-shaft systems, it is conventional to use Ω as the rotational speed of the first shaft (input shaft) of the system. Therefore, it is necessary to use the velocity ratio η to account for the gearing ratio and hence the difference in angular velocities between the shafts. For this purpose, a velocity ratio matrix $[\eta]$ is created, which only contains terms on the main diagonal, representing the velocity ratio between the corresponding degree of freedom and the rotational speed of the input shaft.

Additionally, in the presence of hydrodynamic bearings whose stiffness coefficients vary with the rotational speed of the system, for each solution point of the eigenproblem associated with the dynamic matrix $[A]$ of the system, the (previously calculated) coefficients of the bearings must be included.

3.2 Time Response

In this work, time response is obtained using Newmark's time integration method, which is a widely used numerical technique for solving dynamic equations of motion in structural and dynamic analysis. It belongs to the family of implicit time integration methods and is known for its unconditional stability and ability to accurately capture both high-frequency and low-frequency response.

The method is based on approximating the displacement, velocity, and acceleration at each time step using a second-order Taylor series expansion. By introducing two parameters, namely the numerical damping parameter α and the numerical stiffness parameter δ, the Newmark's method allows for control over the numerical dissipation and stability of the solution, and their main equations are given by:

$$\dot{q}_{t+\Delta t} = \dot{q}_t + [(1-\delta)\ddot{q}_t + \delta\ddot{q}_{t+\Delta t}]\,\Delta t \tag{28}$$

$$q_{t+\Delta t} = q_t + \dot{q}_t\Delta t + [(1/2-\alpha)\ddot{q}_t + \alpha\ddot{q}_{t+\Delta t}]\,\Delta t^2 \tag{29}$$

where the equilibrium equation for time $t+\Delta t$ is:

$$[M]\ddot{q}_{t+\Delta t} + ([C] + \Omega[G])\,\dot{q}_{t+\Delta t} + [K]q_{t+\delta t} = \{F\}_{t+\Delta t} \tag{30}$$

The Newmark's method is efficient for solving problems with nonlinear behavior, as it can handle large deformations and nonlinear material responses. The results obtained in this work were calculated using $\alpha = 0.25$ and $\delta = 0.5$.

4. Results and Discussions

In this section, the results obtained for a multi-axis system connected by gearing are presented. The model, shown in Fig 5 is based on the work of Macedo (2017), and the properties of the gearing are as follows:

Table 1: Gearing Properties

Property	Gear 1	Gear 2
Number of Teeth (Z)	50	20
Pitch Diameter	150mm	60mm
Thickness	25mm	25mm
Normal Pressure Angle	20°	20°
Helix Angle	30°	30°

The results are compared when the system is supported on roller bearings, and journal bearings. Bearing data are shown in tables 2 and 3 respectively.

Table 2: Roller Bearing Properties

$K_{xx} = K_{yy}$	7e7 N/m
$K_{xy} = K_{yx}$	0 N/m
$C_{xx} = C_{yy}$	125 N.s/m
$C_{xy} = C_{yx}$	0 N.s/m

Table 3: Journal Bearing Properties

Bearing Length	25 mm
Bearing Diameter	50 mm
Radial Clearance	100 μm
Absolute viscosity	70 mPa.s

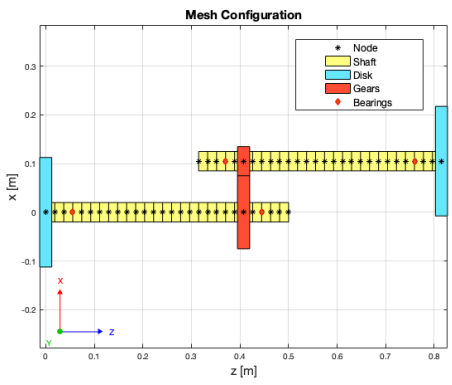

Figure 5: Multi shaft system mesh configuration

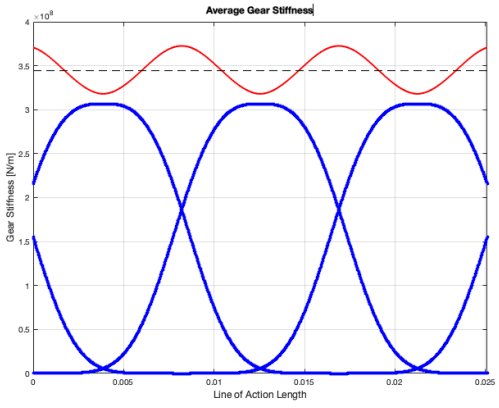

Figure 6: Average gear contact stiffness

Considering the time-varying stiffness of the gearing system, whose profile is illustrated in Figure 6, the temporal integration of the system is performed using the Newmark's method to obtain the time response of the system. Due to the variation in the gearing stiffness, which occurs in this case at a frequency 50 times higher than the rotation speed of the first shaft, it is necessary to use a time integration step of $dt = 1e{-}5$ seconds. Furthermore, to eliminate the influence of transient behavior on the response, the simulation is conducted from 0 to 20 seconds, but only the last 2 seconds are stored and saved for analysis.

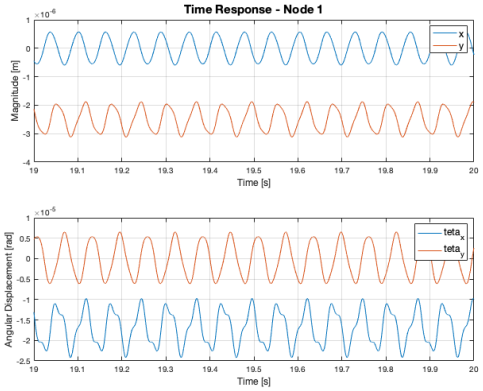

(a) Roller Bearings

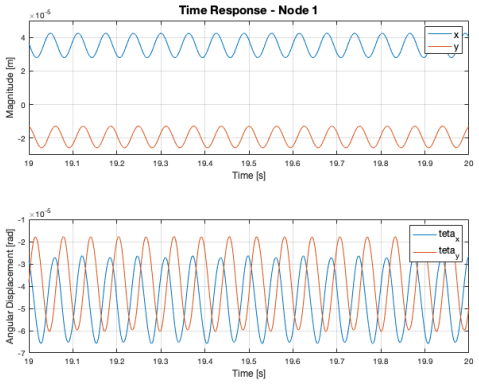

(b) Hydrodynamic Bearings

Figure 7: Time response comparison on node 1 - first shaft disk

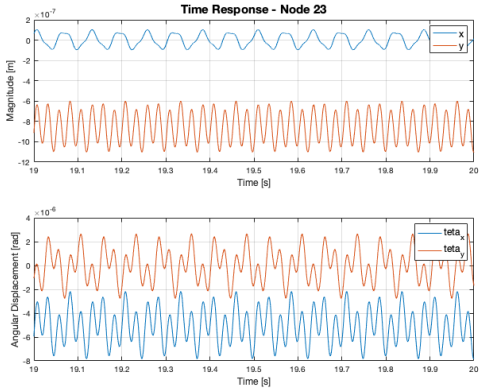

(a) Roller Bearings

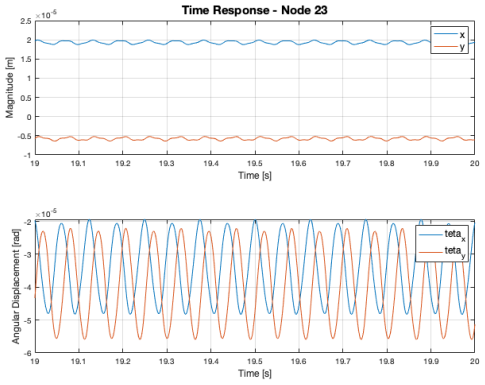

(b) Hydrodynamic Bearings

Figure 8: Time response comparison on node 23 - first shaft disk

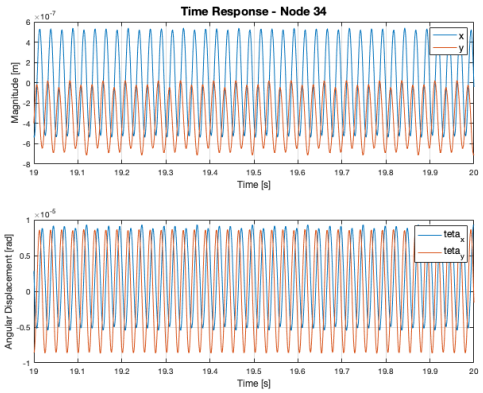

(a) Roller bearings

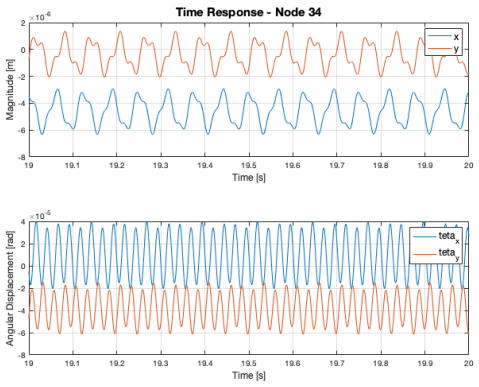

(b) Hydrodynamic Bearings

Figure 9: Time response comparison on node 34 - second shaft gear

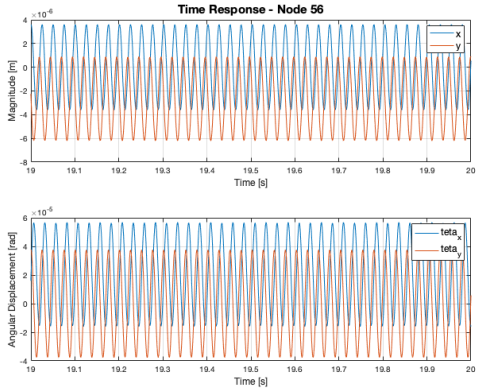

(a) Roller bearings

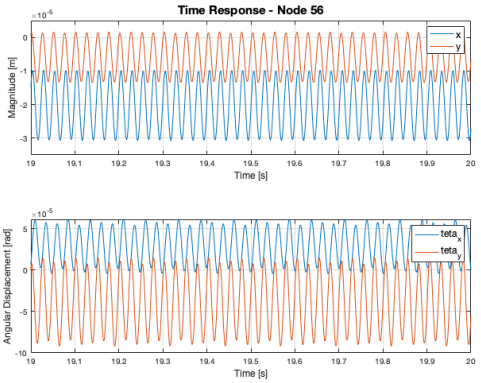

(b) Hydrodynamic bearings

Figure 10: Time response comparison on node 56 - second shaft disk

It is possible to observe that the signals of the time response exhibit a composition of different frequencies, particularly at the gear nodes. For this reason, the signals are also analyzed in frequency domain, applying the Fast Fourier Transform (FFT) in the time responses.

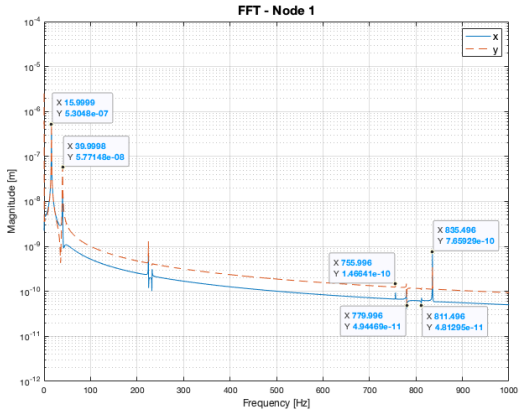

(a) Roller bearings

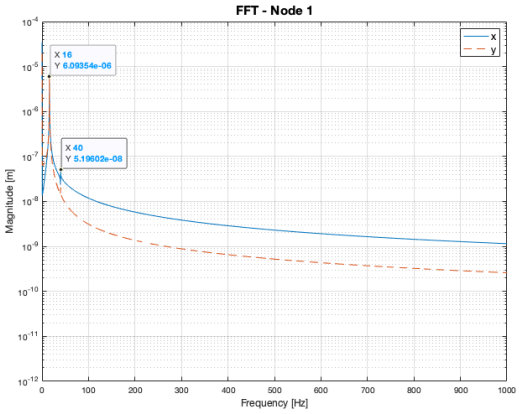

(b) Hydrodynamic bearings

Figure 11: FFT on time response on node 1 comparison - first shaft disk

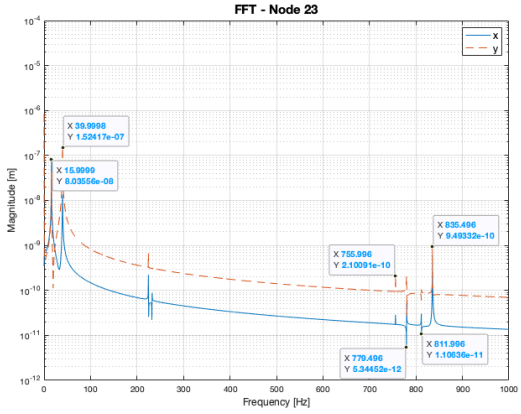

(a) Roller bearings

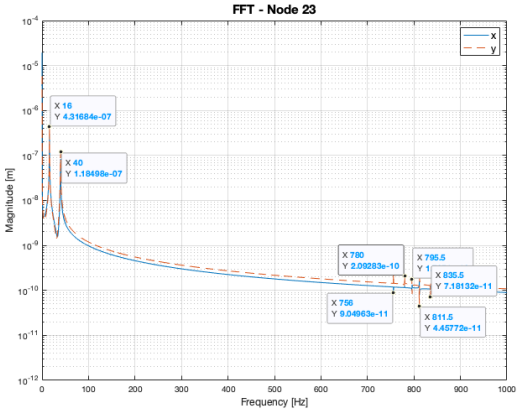

(b) Hydodrynamic bearings

Figure 12: FFT on time response on node 23 comparison - first shaft gear

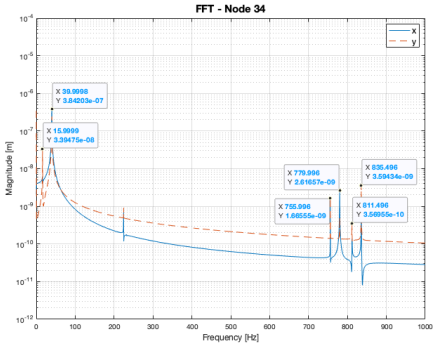

(a) Roller bearings

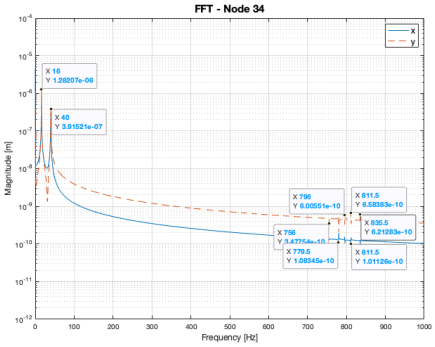

(b) Hydrodynamic bearings

Figure 13: FFT on time response on node 34 comparison - second shaft gear

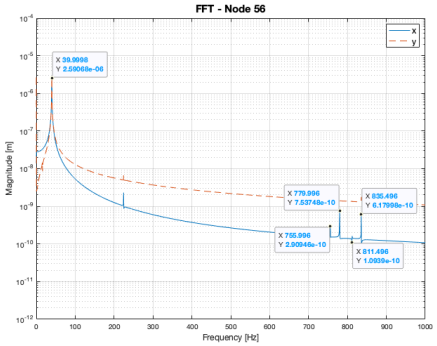

(a) Roller Bearings

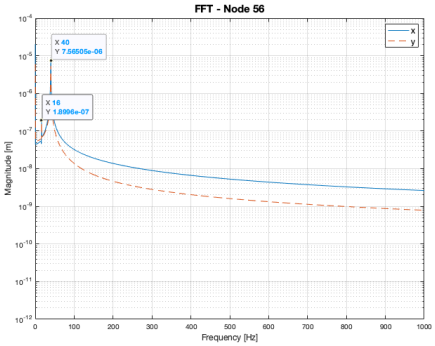

(b) Hydrodynamic bearings

Figure 14: FFT on time response on node 56 comparison - second shaft disk

The analysis of the spectrum of the time signals indicates two frequencies at approximately 16 and 40 Hz, which correspond respectively to the rotation frequencies of the first and second shafts, since in this simulation the input shaft rotates at $\Omega = 100$ rad/s, equivalent to 16 Hz. The frequency of 40 Hz arises from the gearing engagement between the shafts, which have a gear ratio of 1:2.5. Moreover, the rotation frequencies of each shaft are more prominent at the nodes of their respective disks, while at the gear nodes, both frequencies are identified with significant signal amplitude.

Another important point is the identification of frequencies around 796 Hz. Given that the input shaft rotates at $\Omega = 100$ rad/s and its gear has 50 teeth, the gear frequency can be inferred as $\Omega_g = 50 \times 100 = 500$ rad/s = 795.7 Hz. This frequency precisely corresponds to the oscillation frequency of the gear pair stiffness signal (Figure 6). For both bearings, two pairs of frequencies are observed: Pair 1 - 756 and 835.5 Hz, corresponding to $\Omega_g \pm 39.5$ Hz; Pair 2 - 780 and 811 Hz, corresponding to $\Omega_g \pm 15.5$ Hz.

The ratio between the distances of each frequency pair is approximately equal to the gear ratio ($39.5/15.5 \approx 2.5$), suggesting that these pairs represent harmonic frequencies of the gearing and its frequency Ω_g.

For the frequency analysis, a gear element with constant stiffness was used, obtained from the average tooth contact stiffness. Thus, it was possible to determine the Campbell Diagram of the invariant system. These results are presented below, comparing the results obtained for the system supported by rolling bearings and supported by journal bearings.

Finally, the results presented indicate that, in general, the amplitudes of the signals are smaller for the cases with hydrodynamic bearings compared to rolling bearings. This phenomenon is related to the damping of the bearings, which in this specific case indicates higher damping values for the hydrodynamic bearing case. Therefore, it is suggested that the correct sizing of this type of bearing may influence the dynamic response of the system.

The comparison between figures 15a and 15b reveals that the type of bearing has a significant influence on the natural frequencies of the system. The first observation that can be made is regarding the free body modes, which are identified in the Campbell diagram of the case with hydrodynamic bearings by the curves whose natural frequency starts at 0 Hz and increases. This type of phenomenon is typically observed in rotating systems supported by hydrodynamic bearings, due to the high values of stiffness and damping coefficients at low rotational speeds.

Additionally, it can be observed that two of the natural frequency curves exhibited similar behavior between the two tested cases. One of the curves that starts at 0 Hz begins to show similar behavior to the case with rolling element bearings when the rotational speed exceeds 9000 RPM, while the others exhibit quite distinct behavior.

Finally, in the Campbell diagram for the system with hydrodynamic bearings, at least one of the natural frequency

curves draws attention as it closely follows the 1x reference curve of the first shaft. It is important to observe the type of mode that this curve represents and whether it is predominant in a specific rotor or occurs in both rotors of the system.

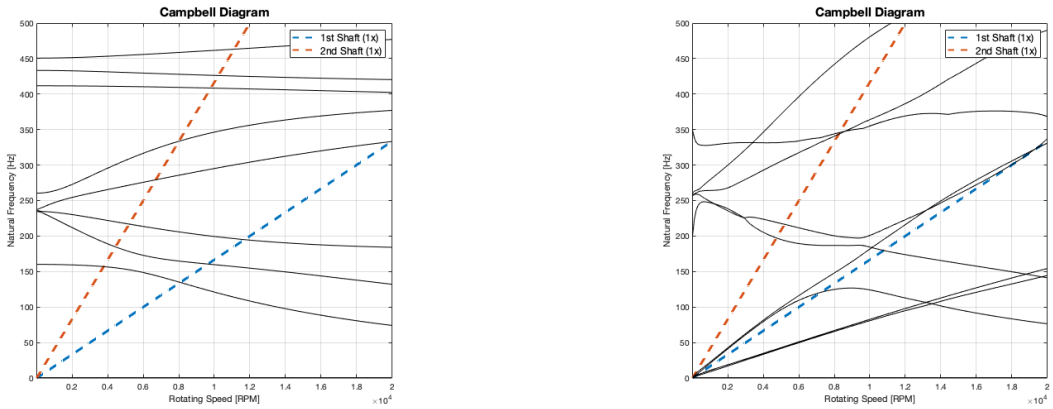

(a) Roller bearings (b) Hydrodynamic bearings

Figure 15: Comparison of the Campbell Diagram for rolling element bearings and hydrodynamic bearings in a multi-axis system with constant stiffness gearing.

5. Conclusions

In this work, a MATLAB® program was developed to simulate a horizontal wind turbine like rotor dynamics system using the Finite Element Method, allowing for modal analysis, unbalance response, and time integration. The program includes simple coefficient bearing elements as well as hydrodynamic bearings, enabling the comparison of the bearing effects on the system. Additionally, the program allows for the simulation of multi-axis systems connected by gears, which are modeled using the formulation proposed by Cai (1995).

Results obtained suggest that the type of bearing used in the system has a significant influence on its natural frequencies and Campbell diagram, although this may also depend on the correct sizing and selection of bearing parameters. Another interesting result is that the temporal response signals are composed of multiple frequencies, which are not limited to the rotational frequencies of the two shafts but also include the gear meshing frequency and its harmonics.

6. REFERENCES

Agência Nacional de Energia Elétrica, 2005. *Atlas de energia elétrica do Brasil*. 2nd edition.

Ansys, 2018. "Mechanical apdl element reference, release 18.1".

Associação Brasileira de Energia Eólica e Novas Tecnologias, 2021. "Boletim anual 2021". Technical report.

Bloomberg New Energy Finance, 2021. "New energy outlook 2021". Technical report.

Cai, Y., 1995. "Simulation on the rotational vibration of helical gears in consideration of the tooth separation phenomenon (a new stiffness function of helical involute tooth pair)". *Journal of Mechanical Design*, Vol. 117, No. 3, pp. 460–469.

Global Wind Energy Council, 2021. "Global wind report 2021". Technical report.

He, S., Gunda, R. and Singh, R., 2007. "Effect of sliding friction on the dynamics of spur gear pair with realistic time-varying stiffness". *Journal of Sound and Vibration*, Vol. 301, No. 3-5, pp. 927–949.

Kramer, E., 1993. *Dynamics of rotors and foundations*. Springer.

Kubur, M., Kahraman, A., Zini, D.M. and Kienzle, K., 2004. "Dynamic analysis of a multi-shaft helical gear transmission by finite elements: Model and experiment". *Journal of Vibration and Acoustics*, Vol. 126, No. 3, pp. 398–406.

Macedo, B.O., 2017. *Estudo do Comportamento Vibratório Lateral e Torcional do Trem de Potência de um Aerogerador de Eixo Horizontal*. Dissertação de mestrado, Faculdade de Engenharia Mecânica.

Nelson, H.D., 1980. "A finite rotating shaft element using timoshenko beam theory". *Journal of Mechanical Design*, Vol. 102, No. 4, pp. 793–803.

Pinto, R.J. and dos Santos, V.M.L., 2019. "Energia eólica no brasil: Evolução, desafios e perspectivas". *Journal on Innovation and Sustainability*, Vol. 10, No. 1, pp. 124–142.

Rao, J., Shiau, T. and Chang, J., 1998. "Theoretical analysis of lateral response due to torsional excitation of geared rotors". *Mechanism and Machine Theory*, Vol. 33, No. 6, pp. 761–783.

Visnadi, L.B., 2022. *Efeito de trinca em engrenagens de dente reto na resposta dinâmica do rotor*. Tese de doutorado, Faculdade de Engenharia Mecânica.

7. RESPONSIBILITY NOTICE

The authors are solely responsible for the printed material included in this paper.